Hindawi

*Research Article*

# Multiobjective Optimization of Stress-Release Boot of Solid Rocket Motor under Vertical Storage Based on RBF Model

**Qiuwen Miao** [1,2] **Huihui Zhang,** [1,2] **Zhibin Shen** [1,2] **and Weiyong Zhou** [1,2]

[1] *College of Aerospace Science and Engineering, National University of Defense Technology, Changsha, Hunan 410073, China*
[2] *Hunan Key Laboratory of Intelligent Planning and Simulation for Aerospace Missions, Changsha, Hunan 410073, China*

Correspondence should be addressed to Zhibin Shen; zb_shen@yeah.net

Stress-release boot can effectively improve the structural integrity of SRM (solid rocket motor), but it will also influence the loading fraction and interior ballistic performance, so the purpose of this paper is to propose a multiobjective optimization method for stress-release boot. The design variables are the front and rear depth of the stress-release boot, and four optimization variables were determined according to the analysis of SRM performance. To optimize a SRM with star and finocyl grain, the RBF (radial basis functions) model that satisfies the accuracy requirements was established based on parametric modeling technology and the OPLHS (Optimal Latin Hypercube Sampling) method. Subsequently, the Pareto front was obtained based on the NCGA-II algorithm. And an optimal solution was obtained based on the evolutionary algorithm and weighted method. Compared with the initial SRM, the maximum Von Mises strain of the grain, the maximum principal stress of the insulator/cladding interface, the maximum axial displacement, and the volume increment decreased by 19.92%, 35.33%, 4.80%, and 4.42%, respectively. The optimization design method proposed in this paper has significant advantages in computational efficiency for the optimization of SRM and can take into account various performances of SRM, which not only is suitable for the optimization design of stress-release boot but also provides guidance for the optimization design of other shape parameters of SRM.

## 1. Introduction

Recent developments in the long-range, cross-regional missile weapon system put forward the performance requirements of high loading fraction, long life, and high reliability for SRM [1–3]. However, SRM usually undergoes several load processes of solidification, transport vibration, long-term storage, and internal pressure of ignition during its service life [4]. Under various loads, the structural response of the SRM will occur, including stress, strain, and deformation. Excessive strain will cause dehumidification phenomena and even cracks in the propellant of the SRM grain [5]. Excessive stress will cause debonding at the interface [6, 7] and promote the aging effect of the propellant [8]. Excessive deformation will change the interior ballistic performance of the SRM and reduce its safety at the moment of ignition [9, 10]. Due to the requirement for the high loading fraction of SRM, its structural integrity is exposed to more severe challenges. Therefore, there is an urgent need to improve the optimization design ability of the SRM and develop an optimization design method that takes into account the various performance and optimization efficiency of the SRM [11].

In this paper, the stress-release boot of SRM under vertical storage has been optimized. Stress-release boot can effectively improve the structural integrity of the SRM under solidification load [12, 13]. Zhang et al. [14] analyzed the influence of the stress-release boot by numerical calculation and found that the maximum Von Mises strain of grain decreased from 30.1% to 23.0%. Meng et al. [15, 16] not only established and analyzed the finite element models of the SRM grain with debonded cracks, the result showing that the most dangerous position is the front debonded cracks of the stress-release boot, but also analyzed the change law of the maximum Von Mises strain of the parachute disk engine under different debonding depths. On that basis, the best debonding depth of the stress-release boot was selected according to the production practice.

Li et al. [17] analyzed and summarized the influence of different umbrella slot depths and debonding depths on the maximum Von Mises strain of SRM grain under temperature load. For optimization based on the agent model, Dai et al. [18] analyzed the applicability of the different surrogate model to the optimal problem of semifinishing. Results show that the maximum relative errors based on the RBF model are minimum. Li et al. [19] realized real-time and high-quality control with the help of the RBF model for the optimal control problem for satellites.

From the above introduction, we can observe the number of literature about stress-release boot published. These studies have summarized some of the influence laws of the different depths of stress-release boot on SRM. However, most research to date has tended to focus on the analysis of the strain variation of the SRM grain under temperature load rather than the various performances of the SRM, such as the structural integrity, loading fraction, and interior ballistic performance, and little attention has been paid to building a complete and effective optimization design process.

The central thesis of this paper is to build a complete and effective optimization design process for the SRM with stress-release boot, which could consider the structural integrity, loading fraction, and interior ballistic performance of SRM. In order to optimize the SRM under solidification and vertical storage load, the design variables of the optimization model are determined as the front and rear debonding depths of the stress-release boot, and then, four optimization variables have been determined in accordance with the analysis of the association between structural responses and structural integrity, loading fraction, and interior ballistic performance of the SRM. Afterwards, the radial basis function (RBF) model satisfying the accuracy requirements was established, while the sample data was obtained based on the OPLHS method and parametric modeling technology. Finally, the stress-release boot of a SRM is optimized with two multiobjective optimization methods of nonnormalization and normalization on the basis of the RBF model.

## 2. Model and Methods

*2.1. Model and Design Variables.* A SRM with star and finocyl grain is selected for analysis, and the design variables are $h_f$ and $h_r$, where $h_f$ is the front depth of stress-release boot and $h_r$ is the rear depth in this paper. For the initial SRM, $h_f = 0.89R$ and $h_r = 0.76R$, where $R$ is the radius of the SRM case. The geometric model of the SRM with initial stress-release boot is shown in Figure 1.

In order to improve the calculation efficiency and eliminate the interference caused by human factors, the parametric modeling technology was introduced to implement the automatic simulation analysis of the SRM. According to the cycle symmetry, the 1/12 model of SRM is used for analysis. After grid independence verification and considering the computation cost, the number of grids is controlled at about 30,000.

The simulation analysis sets two steps: the first step is the solidification cooling analysis step. The temperature of the simulation model will be reduced from zero stress temperature of 58°C to room temperature of 20°C during the first

step, while the analysis time was set as 86400 s; the second analysis step is the gravity load analysis step corresponding to the vertical storage; an axial acceleration load of 1 g will be applied to the simulation model during the second step, while the analysis time was set as one month.

According to the cyclic symmetry of the SRM, the symmetric displacement constraint is applied on both sides of the SRM, and then, the axial displacement constraint is applied on the interface between the rear head and the straight cylinder section of the SRM case.

The material parameters of the SRM case, insulator layer, cladding layer, and grain are shown in Table 1, while the relaxation modulus of the viscoelastic propellant is characterized in the form of the Prony series, as shown in Equation (1), where the first eleven-order parameters and relaxation modulus are shown in Table 2.

The WLF equation for the time-temperature equivalent factor of propellant material is in formula (2). In the formula, $C_1$ and $C_2$ are material constants, which are determined by the characteristics of the material itself, in this case, $C_1 = 4.971$, $C_2 = 156.1$, and $T_0$ is the reference temperature, where $T_0 = 293.15$ K:

$$E(t) = E_\infty + \sum_{i=1}^{n} E_i e^{-t/\tau_i}, \tag{1}$$

$$\lg \alpha_T = \frac{-C_1(T - T_0)}{C_2 + (T - T_0)}. \tag{2}$$

*2.2. Optimization Variable.* In order to consider the structural integrity, loading fraction, and interior ballistic performance while optimizing the design of the SRM, the structural response that can effectively reflect the performance of the SRM should be selected as the optimization variables.

First of all, the structural response used to reflect the structural integrity of the engine is considered. The structural integrity problem of the SRM refers to the crack on the grain, debonding at the interface, and excessive deformation of the parts of the SRM under various loads.

It is necessary to analyze the damage of grain propellant under load to judge whether there is a crack. Due to the fact that the propellant will be at a low strain rate if the SRM grain is under solidification and gravity load, dehumidifying is the main damage form for the propellant in this paper. Therefore, it is more appropriate to adopt the damage criterion of octahedral shear strain: $r_8 \leq r_{8m}/n$, where $r_{8m}$ is the critical value and $n$ is the safety factor. The expression of the octahedral shear strain is

$$r_8 = \frac{2}{3}\sqrt{(\varepsilon_x - \varepsilon_y)^2 + (\varepsilon_y - \varepsilon_z)^2 + (\varepsilon_z - \varepsilon_x)^2 + 6\left(\varepsilon_{xy}^2 + \varepsilon_{yz}^2 + \varepsilon_{zx}^2\right)}. \tag{3}$$

In addition, the expression of Von Mises strain is

$$\varepsilon_v = \frac{\sqrt{2}}{3}\sqrt{(\varepsilon_x - \varepsilon_y)^2 + (\varepsilon_y - \varepsilon_z)^2 + (\varepsilon_z - \varepsilon_x)^2 + 6\left(\varepsilon_{xy}^2 + \varepsilon_{yz}^2 + \varepsilon_{zx}^2\right)}. \tag{4}$$

Therefore, $\varepsilon_v = \sqrt{2}/2 r_8$, so the maximum Von Mises strain $\varepsilon_{v\,\max}$ in the grain is used as the structural response
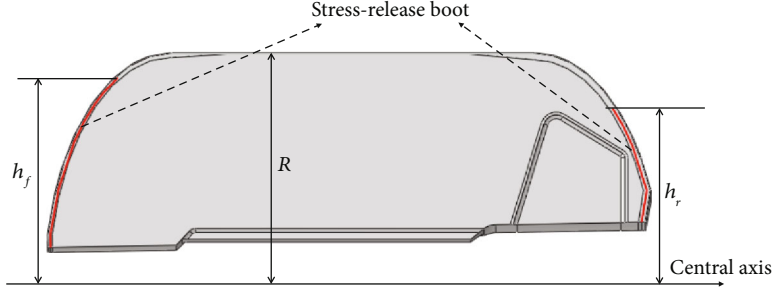
FIGURE 1: Geometric model of the SRM with star and finocyl grain.

TABLE 1: Material parameters of the SRM.

| Material parameters | Elastic modulus (MPa) | Poisson's ratio | Density (kg/m³) | Expansion coefficient (°C⁻¹) |
|---|---|---|---|---|
| Case | $1.86 \times 10^5$ | 0.300 | $7.9 \times 10^3$ | $1.10 \times 10^{-5}$ |
| Insulator | 60.00 | 0.498 | $2.1 \times 10^3$ | $2.20 \times 10^{-5}$ |
| Cladding | Prony series | 0.498 | $1.86 \times 10^3$ | $8.60 \times 10^{-5}$ |
| Propellant | Prony series | 0.498 | $1.86 \times 10^3$ | $8.60 \times 10^{-5}$ |

to reflect whether the column will appear damaged or cracked.

One of the deep-seated reasons for the debonding at the grain/cladding interface is that the stress in the interface caused by the various loads will continuously promote the damage of the interface and the aging of the propellant, until finally the debonding of the interface occurs. Therefore, the maximum principal stress in the grain/cladding interface is used as the structural response data to reflect whether the grain/cladding interface debonding will take place.

Excessive deformation will not only affect the interior ballistic performance of the combustion period of SRM but also affect its safety at the ignition moment. Through the simulation analysis, it can be observed that the obvious creep deformation of the SRM grain will take place during the vertical storage. The front stress-release boot expands continuously under the solidification and gravity load, while the maximum axial displacement is located at the starting position of the front stress-release boot. Therefore, $u_z$, the axial displacement of the starting position of the front stress-release boot, is used as the structural response index to reflect the deformation of the SRM.

Finally, the performance index used to reflect the loading fraction of SRM needs to be considered. The space near the stress-release boot will be filled with high-temperature gas after the grain ignition, so the thickness of the insulator layer in the range of debonding depth needs to increase from 1 mm to 23.2 mm, which decreases the volumetric loading fraction of the SRM. Therefore, the volume increment of the insulator layer caused by setting the stress-release boot is taken as the performance index to reflect the volumetric loading fraction of the SRM.

In order to clearly analyze the effect of the depth of the stress-release boot on SRM in the process of optimization design, the four performance indexes, $\varepsilon_{v\,max}$, $\sigma_{max}$, $u_z$, and $V_i$, were normalized as $\bar{\varepsilon}_{v\,max}$, $\bar{\sigma}_{max}$, $\bar{u}_z$, and $\bar{V}_i$, which are determined as the optimization variables of the optimization model. $\bar{\varepsilon}_{v\,max} = \varepsilon_{v\,max}/\varepsilon_{v\,max}^0$, $\bar{\sigma}_{max} = \sigma_{max}/\sigma_{max}^0$, $\bar{u}_{max} = u_{max}/u_{max}^0$, $\bar{V}_i = V_i/V_i^0$, and $\varepsilon_{v\,max}^0$, $\sigma_{max}^0$, $u_{max}^0$, and $V_i^0$ are the performance indexes of initial SRM, while $\varepsilon_{v\,max}^0 = 0.1101$, $\sigma_{max}^0 = 0.0593$ MPa, $u_{max}^0 = 21.1661$ mm, and $V_i^0 = 6.0081 \times 10^6$ mm³.

*2.3. Process of Optimization.* It is a very sophisticated process to manually establish the model, submit the calculation, and extract the result based on CAD/CAE software, not only because of the complexity of the SRM structure but also because of the randomness of the results caused by the intervention of human factors. In order to use parameters to drive the whole numerical process automatically and then reduce the computation cost of the analysis process, parametric modeling technology was introduced into the analysis process of the SRM, which could decrease the single analysis time from about 1 day to about 15 minutes.

Besides, it is usually necessary to modify the design variables thousands of times and obtain the structural response data in the optimization design, so the surrogate model technology was adopted to ensure that the optimization design is carried out efficiently. The optimization workflow based on the parametric modeling technology and surrogate model is shown in Figure 2.

## 3. Results and Discussion

*3.1. Process of Optimization.* At present, the surrogate models are commonly established based on RSM (Response Surface Methodology), kriging, RBF (radial basis function), and SVR (Support Vector Regression) models. The RBF model is adopted to establish the surrogate model in this paper because it has the advantages of simple structure and fast training speed and is useful in approximating a wide range of nonlinear spaces. The basic mathematical expression of the RBF model is

$$\tilde{f}(x) = \sum_{i=1}^{N} w_i \varphi(\|x - x_i\|), \tag{5}$$

where $w_i$ is the weight coefficient of the $i$th basis function.

In order to establish a RBF model that satisfies the precision requirements after determining its types, the OPLHS

TABLE 2: The first 11-order parameters of Prony series.

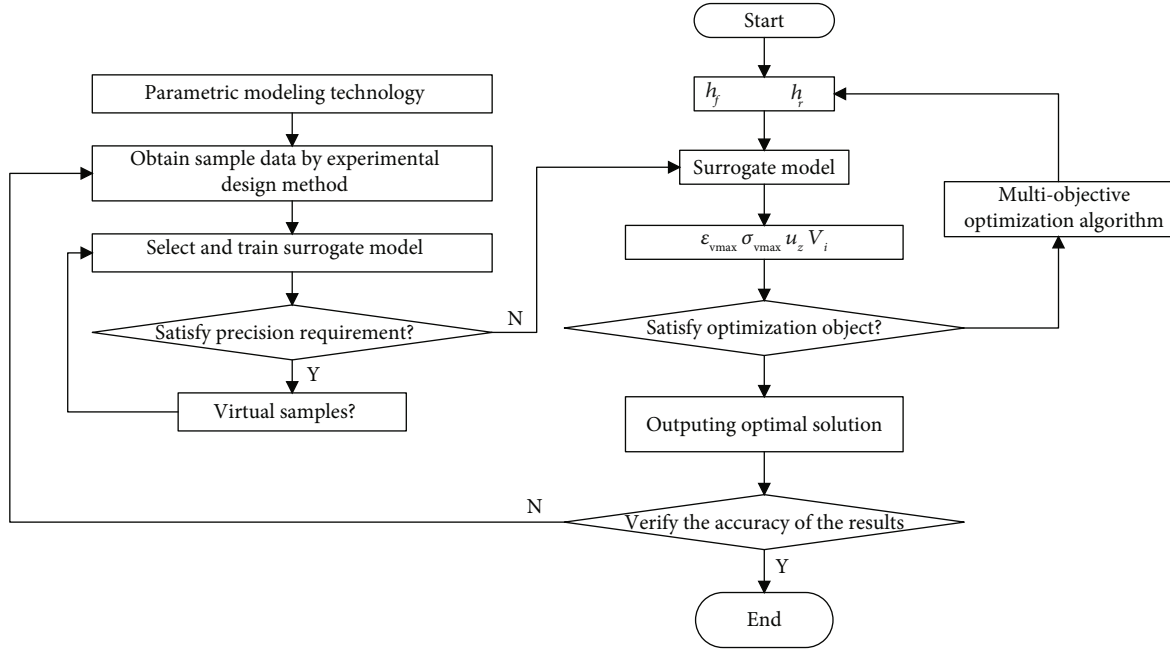| i | 1 | 2 | 3 | 4 | 5 | 6 | 7 | 8 | 9 | 10 | 11 | 12 |
|---|---|---|---|---|---|---|---|---|---|---|---|---|
| $\tau_i$ | 0.012 | 0.149 | 1.797 | 21.57 | 258.8 | 3106 | 37278 | $4 \times 10^{-5}$ | $4 \times 10^{6}$ | $4 \times 10^{7}$ | $4 \times 10^{8}$ | $\infty$ |
| $E_i$ | 20.48 | 5.532 | 4.246 | 3.427 | 1.564 | 0.050 | 0.721 | 0.101 | 0.049 | 0.039 | 0.031 | 0.719 |



FIGURE 2: Flow chart of optimization based on parametric modeling technology and a surrogate model.

method was used to collect 300 sets of sample data in the design space of $\{(h_f, h_r) | h_f \in [0.26R, 0.98R], h_r \in [0.45R, 0.95R]\}$, and an initial RBF model was established on the basis of the 300 sets of sample data, while the 300 sampling points are shown in Figure 3(a). But the preliminary test results show that the prediction accuracy of the surrogate model is low when $h_f$ and $h_r$ are large, so the range of $\{(h_f, h_r) | h_f \in [078R, 0.98R], h_r \in [0.75R, 0.95R]\}$ is encrypted locally. Finally, 366 groups of sample data sampling points were collected, and the schematic diagram is shown in Figure 3(b).

In order to verify the effectiveness and accuracy of the RBF model, two groups of data in two ranges were randomly sampled, where the first data group was $h_f \in [0.26R, 0.98R]$ while $h_f = 0.89R$, and the second data group was $h_r \in [0.45R, 0.95R]$ while $h_r = 0.76R$, and then, the prediction results of the RBF model were compared with the actual calculation results. The comparison results are shown in Figure 4.

According to the comparative result, it can be observed that the structural response predicted by the RBF model after modification is in high coincidence with the calculation results, and its accuracy satisfies the requirements. In addition, the influence law can also be reached from Figure 4: for the SRM under vertical storage, the structural integrity performance index is sensitively affected by the front debonding depth of the stress-release boot, while the rear debonding depth can affect structural integrity slightly.

3.2. Multiobjective Optimization Based on NCGA-II. Multiobjective optimization was carried out based on the NCGA-II algorithm in order to obtain a Pareto front. Compared with the NCGA algorithm, the NCGA-II algorithm proposed the concept of fast nondominated sorting, which can reduce the computational complexity. And the new population comes from the population after the combination of father and progeny populations, which can retain the existing optimal solution and ensure the convergence of the algorithm in the continuous process of population renewal. In addition, the crowding operator is added to obtain a more uniform Pareto front. The optimization process based on the NCGA-II algorithm is shown in Figure 5.

For the optimization design of a SRM, the strain, stress, and deformation under load should be reduced while the loading fraction of the SRM should be increased as much as possible. So, the mathematical expression of the optimization problem is

$$
\begin{cases}
\text{Minimize } \bar{\varepsilon}_{v\max}(h_f, h_r), \\
\text{Minimize } \bar{\sigma}_{\max}(h_f, h_r), \\
\text{Minimize } \bar{u}_{\max}(h_f, h_r), \\
\text{Minimize } \overline{V_i}(h_f, h_r) \\
\text{s.t.} \{(h_f, h_r) | h_f \in [0.26R, 0.98R], h_r \in [0.45R, 0.95R]\}.
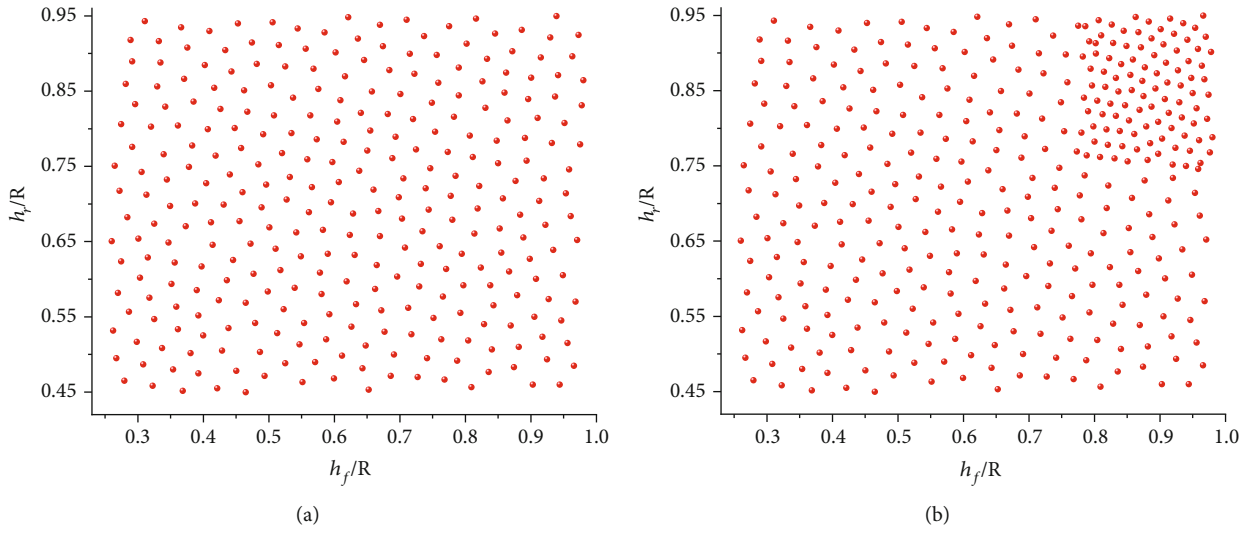\end{cases} \tag{6}
$$

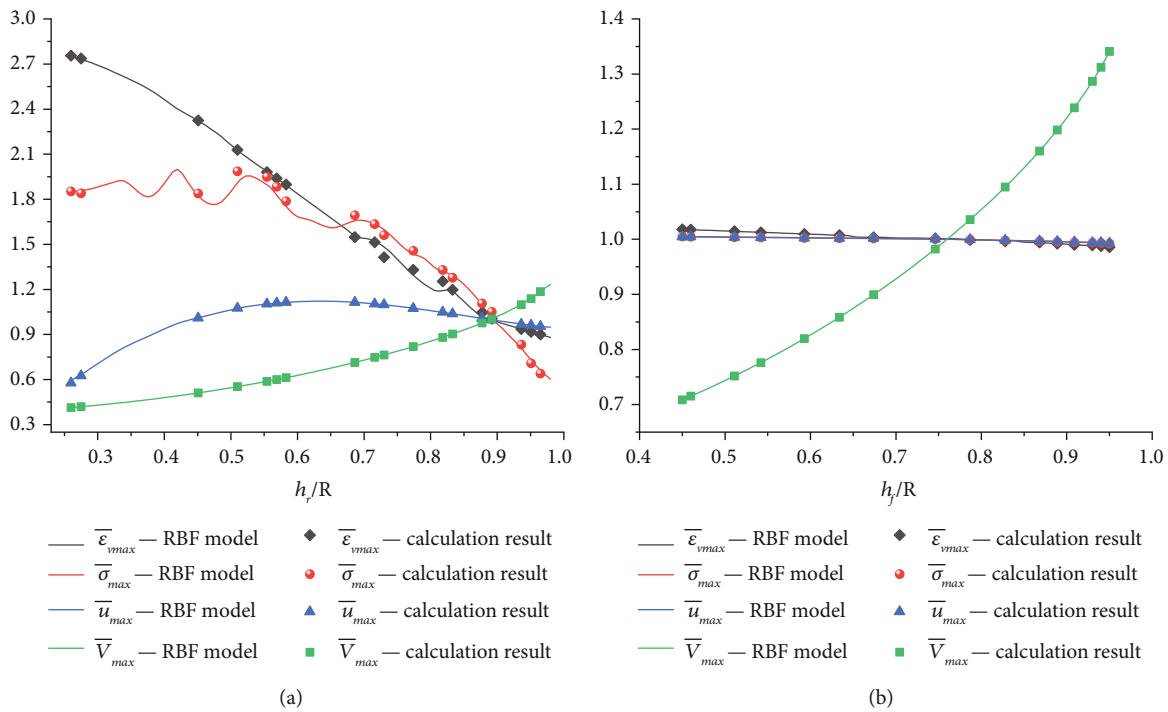FIGURE 3: Schematic diagram of sampling points based on the OPLHS method.



FIGURE 4: Comparison chart between the RBF model and the calculation results.

In order to more intuitively observe the state of the Pareto front, the performance indexes related to the structural integrity of SRM as $\bar{\varepsilon}_{v\,max}$, $\bar{\sigma}_{max}$, and $\bar{u}_{max}$ are merged into one performance index as $f(h_f, h_r) = \{\bar{\varepsilon}_{v\,max} + \bar{\sigma}_{max}(h_f, h_r) + \bar{u}_{max}(h_f, h_r)\}/3$, while the NCGA-II algorithm is used to optimize, the number of primary populations is set to 60, and the reproductive generation is set to 100.

The optimization calculation time based on the RBF model is less than one minute, and then, the Pareto solution is drawn as shown in Figure 6(a), the partial Pareto front is shown in Table 3, and the distribution data of the optimization variables are shown in Figure 6(b).

It can be observed that the Pareto front is mainly distributed in two regions: the first is that the front debonding depth is large and the rear debonding depth is small, while $\bar{\varepsilon}_{v\,max}$, $\bar{\sigma}_{max}$, and $\bar{u}_{max}$ are smaller compared with the initial SRM, and $\overline{V_i}$ does not change much. The second is that the front and rear debonding depths are both small, while $\overline{V_i}$ decreases a lot compared with the initial SRM, but $\bar{\varepsilon}_{v\,max}$, $\bar{\sigma}_{max}$, and $\bar{u}_{max}$ become larger than before.
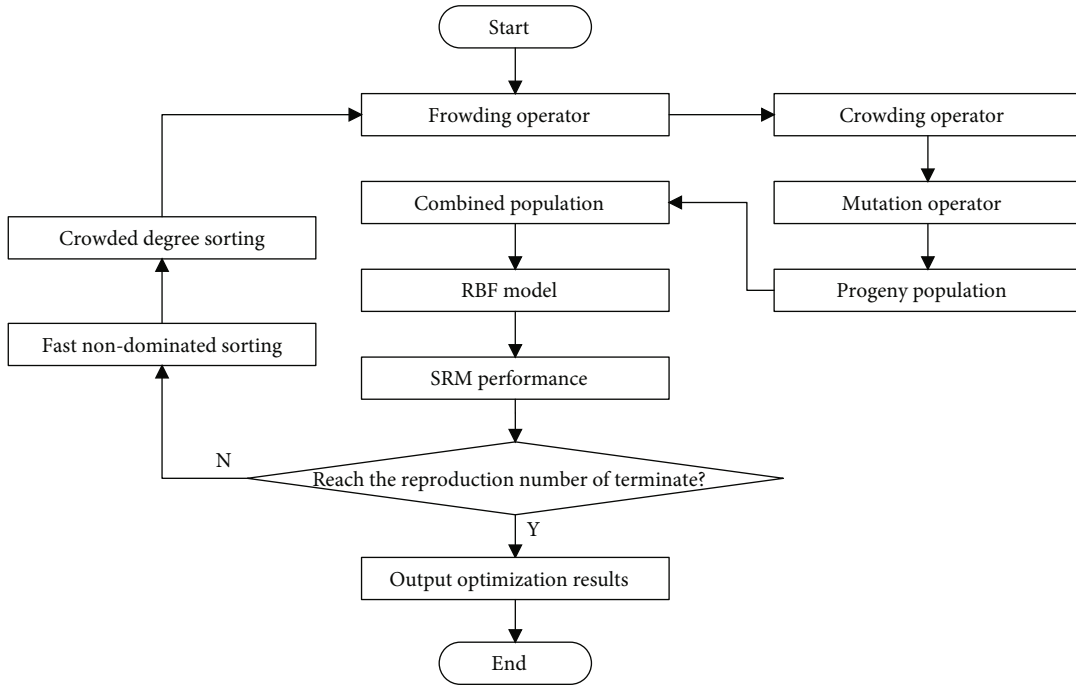
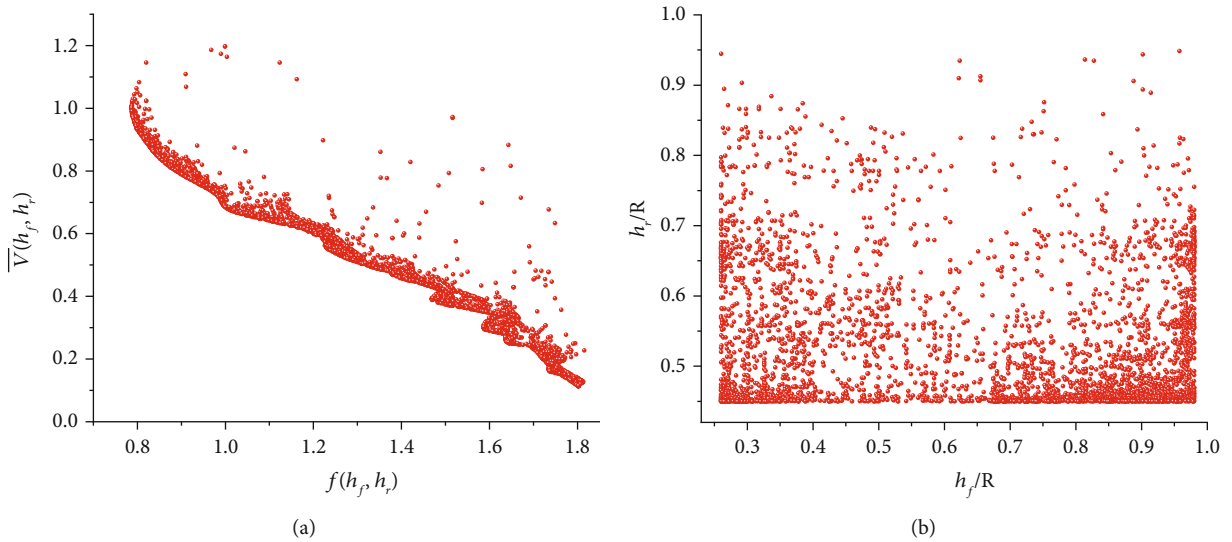FIGURE 5: Flow chart of optimization based on the NCGA-II algorithm.



(a)



(b)

FIGURE 6: Diagram of optimization results based on NCGA-II algorithm.

### 3.3. Multiobjective Optimization Based on the Evolutionary Algorithm.

The multiobjective optimization algorithm can be divided into normalization and nonnormalization algorithms. The nonnormalization method can obtain the Pareto front of the optimization problem. And since the normalization method can convert multiple objectives into a single objective, the designer can determine the weight coefficient of each optimization variable according to the performance demand and their importance. And then, one of the Pareto fronts can be quickly obtained on the basis of the direction in the target space determined by the weight coefficient. Therefore, the multiobjective optimization design problem

of the stress-release boot of SRM is transformed into a single-objective optimization design problem by the weighting method, and its mathematical expression is

$$
\begin{cases}
\text{Minimize}\left\{\omega_1\bar{\varepsilon}_{v\,\max}(h_{\mathrm{f}}, h_{\mathrm{b}}) + \omega_2\bar{\sigma}_{\max}(h_{\mathrm{f}}, h_{\mathrm{r}}) + \omega_3\bar{u}_{\max}(h_{\mathrm{f}}, h_{\mathrm{r}}) + \omega_4\bar{V}(h_{\mathrm{f}}, h_{\mathrm{r}})\right\} \\
\text{s.t.}\left\{(h_{\mathrm{f}}, h_{\mathrm{b}})|h_{\mathrm{f}} \in [0.26R, 0.98R], h_{\mathrm{r}} \in [0.45R, 0.95R]\right\},
\end{cases}
\tag{7}
$$

where $\omega_1$, $\omega_2$, $\omega_3$, and $\omega_4$ are the weight coefficients of $\varepsilon_{v\,\max}$, $\sigma_{\max}$, $u_z$, and $V_i$.

TABLE 3: Value of performance index under a different stress-release boot.

| Type | $h_f$ | $h_r$ | $\bar{\varepsilon}_{v\,max}$ | $\bar{\sigma}_{max}$ | $\bar{u}_{max}$ | $\overline{V}_i$ | $f(h_f, h_b)$ |
|---|---|---|---|---|---|---|---|
| Initial | 0.890 | 0.760 | 1.000 | 1.000 | 1.000 | 1.000 | 1.000 |
| | 0.293 | 0.450 | 2.689 | 1.949 | 0.722 | 0.137 | 1.787 |
| | 0.301 | 0.450 | 2.677 | 1.923 | 0.738 | 0.140 | 1.779 |
| | 0.308 | 0.450 | 2.665 | 1.907 | 0.754 | 0.143 | 1.775 |
| Partial Pareto front | 0.563 | 0.486 | 1.831 | 1.865 | 1.127 | 0.329 | 1.607 |
| | 0.965 | 0.460 | 0.810 | 0.695 | 0.957 | 0.897 | 0.821 |
| | 0.965 | 0.478 | 0.806 | 0.683 | 0.956 | 0.911 | 0.815 |
| | 0.980 | 0.470 | 0.803 | 0.653 | 0.953 | 0.944 | 0.803 |
| | 0.980 | 0.476 | 0.802 | 0.650 | 0.952 | 0.949 | 0.802 |
| Final | 0.980 | 0.485 | 0.801 | 0.647 | 0.952 | 0.956 | 0.800 |

Actually, stress and strain are two of the most concerning performance indicators for designers because they are directly related to the structural safety of the SRM, so $\omega_1$ and $\omega_2$ were set as 0.3, and $\omega_3$, $\omega_4$ were set as 0.2.

And then, the single-objective optimization was carried out on the basis of the evolutionary algorithm. The optimal solution was obtained when $h_f = 0.980$ and $h_r = 0.485$ after 4597 calculations, while $\varepsilon_{v\,max} = 0.0882$, $\sigma_{max}^0 = 0.0383$ MPa, $u_{max}^0 = 20.1508$ mm, and $V_i^0 = 5.7427 \times 10^6$ mm$^3$ and decreased 19.92%, 35.33%, 4.80%, and 4.42% compared with the initial SRM, respectively.

## 4. Conclusion

In this paper, the optimization design of the stress-release boot of SRM was carried out. After analyzing and determining the design variables and optimization variables, the RBF model that satisfies the accuracy requirements was established based on parametric modeling technology and the OPLHS method, and then, the nonnormalized and normalized multiobjective optimization algorithms are used to optimize. The conclusions are as follows:

(1) The optimization design method for the SRM stress-release boot based on parametric modeling technology and surrogate model is proposed, which has significant advantages in computational efficiency. And the optimization design process can take into account the structural integrity, loading fraction, and interior ballistic performance of SRM

(2) Nonnormalized multiobjective design of the stress-release boot was carried out based on the NCGA-II algorithm. The results show that the Pareto solution is mainly distributed in the regions where the front debonding depth is large and the rear debonding depth is small and in the regions where the front and rear debonding depths are both small

(3) The normalized multiobjective design of the stress-release boot was carried out based on the evolutionary algorithm and obtained an optimal solution. Compared with the initial SRM, the maximum Von Mises strain of the grain, the maximum principal stress of the grain/cladding interface, the axial displacement of the starting point of the front stress-release boot, and the volume increment of the insulator layer decreased by 19.92%, 35.33%, 4.80%, and 4.42%, respectively

(4) The optimization design method and process proposed in this paper not only are suitable for the optimization design of the stress-release boot but also provide guidance for the optimization design of other shape parameters of SRM. Based on this, the subsequent research should focus on the shape optimization of the SRM and consider the internal ballistic performance of the SRM more comprehensively in combination with the burning surface regression, so as to provide guidance for the design of the SRM with high loading, long life, and high reliability

## Data Availability

The data used to support the findings of this study are included within the article.

## Conflicts of Interest

The authors declare that they have no conflicts of interest.

## Acknowledgments

## References

[1] R. Marimuthu and B. Nageswara Rao, "Development of efficient finite elements for structural integrity analysis of solid rocket motor propellant grains," *International Journal of Pressure Vessels and Piping*, vol. 111-112, pp. 131–145, 2013.

[2] G. H. Murari, F. L. Calciolari, and L. E. N. de Almeida, "Dynamic mechanical characterization of composite solid propellant for propellant grain structural integrity assessment," *Macromolecular Symposia*, vol. 383, no. 1, p. 1800050, 2019.

[3] Z. Zhang, F. Gao, R. Lv, and Y. Gao, "Coupling of level set and volume of fluid methods for simulations of transient internal flow field in solid rocket motors," *International Journal of Aerospace Engineering*, vol. 2021, 11 pages, 2021.

[4] Z. Wang and Y. Q. Hu, *Solid rocket motor*, China Aerospace Publishing House, Beijing, 1994.

[5] Z. J. Wang, H. F. Qiang, G. Wang, X. C. Liu, and Q. Z. Huang, "Tensile mechanical properties and constitutive model for HTPB propellant at low temperature and high strain rate," *Journal of Propulsion Technology*, vol. 132, no. 24, pp. 1426–1432, 2015.

[6] X. L. Ma, Z. B. Shen, and H. R. Cui, "Simulation and experimental study on mechanical behavior of mode isolid propellant/insulator interface debonding," *Journal of Solid Rocket Technology*, vol. 42, pp. 282–289, 2019.

[7] X. Qiu, G. C. Li, C. L. Zhang, and M. Yang, "Cumulative damage distribution analysis of solid rocket motor interface based on principal stress," *Journal of Solid Rocket Technology*, vol. 37, no. 346-351, p. 375, 2014.

[8] F. T. Zhang, S. Peng, B. L. Sha, and X. H. Chi, "Study on equivalent accelerated test method of low temperature stress for solid propellant charge," *Journal of Solid Rocket Technology*, vol. 42, no. 409-413, p. 418, 2019.

[9] N. Raouf, S. H. Pourtakdoust, B. A. A. Abadi, and A. Rajabi-Ghanavieh, "Structural reliability analysis of solid rocket motor with ellipsoidal cap," *Journal of Spacecraft and Rockets*, vol. 53, no. 2, pp. 389–392, 2016.

[10] X. Wang, R. Y. Zhao, and K. Wang, "Structural finite element analysis of solid motor grain under vertical storage," *Journal of Sichuan Ordnance*, vol. 41, no. 45-51, p. 102, 2020.

[11] A. Kevin, H. Roy, H. Wade, and J. Rhonald, "Solid rocket motor design using hybrid optimization," *International Journal of Aerospace Engineering*, vol. 2012, Article ID 987402, 9 pages, 2012.

[12] T. P. Li, J. L. Han, Y. He, and Y. Guo, "Crack group effect analysis of the stress-release boot of solid rocket motor based on numerical simulation," *International Journal of Aerospace Engineering*, vol. 2021, Article ID 2612441, 9 pages, 2021.

[13] C. Z. Ruan, "Critical techniques in development of large-size solid rocket motors," *Journal of Solid Rocket Technology*, vol. 28, pp. 23–28, 2005.

[14] X. H. Zhang, X. Y. Zheng, H. Y. Li, and Z. Wang, "Stress and strain analysis for solid rocket motor grains with stress-release boot," *Chinses Journal of Applied Mechanics*, vol. 29, pp. 426–430, 2012.

[15] S. Y. Meng, J. L. Han, C. S. Liu, and X. H. Yang, "Stability analysis of cracks in the stress-release boot of solid rocket motor grain with J-integral," *Mechatronics and Materials Processing I, PTS*, vol. 328-330, no. 328-330, pp. 1210–1215, 2011.

[16] S. Y. Meng, G. J. Tang, and Y. J. Lei, "A method of obtaining the suitable debonded length of the stress release boot of solid rocket motor," *Guangxi Sciences*, vol. 2, no. 106-108, p. 112, 2004.

[17] L. Li, Y. J. Lei, Z. B. Shen, and G. J. Tang, "Influence of umbrellar slot depth and debonded depth on strain of grain under temperature load," *Journal of Solid Rocket Technology*, vol. 3, pp. 285–288, 2010.

[18] Y. N. Dai, X. T. Zheng, X. B. Chen, and J. Y. Yu, "A prediction model of milling force for aviation 7050 aluminum alloy based on improved RBF neural network," *The International Journal of Advanced Manufacturing Technology*, vol. 110, no. 9-10, pp. 2493–2501, 2020.

[19] H. J. Li, Y. F. Dong, and P. Y. Li, "Genetic programming method for satellite system topology and parameter optimization," *International Journal of Aerospace Engineering*, vol. 2020, 14 pages, 2020.